

The *Yasone* catalogue: three new Milky Way satellites and 17 further hypercompact candidates

J. Untzaga^{1,2} , M. Mezcua^{1,3} , S. Bonoli^{2,4} , N. Bastian^{2,4} , J. F. Navarro⁵ , S. E. T. Smith⁵ , F. Pérez-Toledo^{6,7} , D. Boyea⁵  *

¹*Institute of Space Sciences (ICE, CSIC), Campus UAB, Carrer de Magrans, 08193 Barcelona, Spain*

²*Donostia International Physics Center (DIPC), Manuel Lardizabal Ibilbidea, 4, San Sebastián, Spain*

³*Institut d'Estudis Espacials de Catalunya (IEEC), Edifici RDIT, Campus UPC, 08860 Castelldefels (Barcelona), Spain*

⁴*IKERBASQUE, Basque Foundation for Science, E-48013, Bilbao, Spain*

⁵*Dept. of Physics and Astronomy, University of Victoria, PO Box 3055, STN CSC, Victoria, BC V8W 3P6, Canada*

⁶*Instituto de Astrofísica de Canarias (IAC), C/Vía Láctea s/n, E-38205 La Laguna, Tenerife, Spain*

⁷*GRANTECAN, Cuesta de San José s/n, E-38712 Breña Baja, La Palma, Spain*

ABSTRACT

We present the discovery of three new low-latitude ($|b| \sim 20^\circ$) Milky Way satellites: *Yasone-1*, *Yasone-2*, and *Yasone-3*. They were identified in our search for compact stellar overdensities in the photometric catalogue of the Panoramic Survey Telescope and Rapid Response System 1, supported by follow-up deep photometric imaging from the Gran Telescopio Canarias OSIRIS instrument and *Gaia* astrometric data. These three new Milky Way satellites are found as compact stellar overdensities that exhibit structural and photometric properties consistent with old, metal-poor populations. All three are best described by isochrone fits corresponding to an age of ~ 12 Gyr and subsolar metallicities: $[\text{Fe}/\text{H}] \sim -1.5$ for *Yasone-1* and *Yasone-2*, and $[\text{Fe}/\text{H}] \sim -2.0$ for *Yasone-3*. *Yasone-1*, located at a heliocentric distance of 12^{+3}_{-2} kpc, has a physical half-light radius of $1.40^{+0.35}_{-0.23}$ pc, an absolute V -band magnitude of $+2.36^{+0.40}_{-0.48}$, and a total stellar mass of $18.2^{+10.2}_{-5.6} M_\odot$. *Yasone-2*, at a distance of 20^{+10}_{-12} kpc, has a slightly larger size of $2.44^{+1.22}_{-1.46}$ pc, a brighter V -band magnitude of $+1.83^{+1.99}_{-0.88}$, and a higher mass of $28.0^{+35.0}_{-23.5} M_\odot$. *Yasone-3*, located at 15^{+3}_{-5} kpc, is the faintest and least massive of the three, with $M_V = +2.52^{+0.48}_{-0.62}$, a stellar mass of $14.4^{+11.2}_{-5.2} M_\odot$, and a half-light radius of $2.09^{+0.70}_{-0.42}$ pc. We also report a fourth (*Yasone-4*), lower-confidence hypercompact candidate located at Galactic latitude $b \sim 48^\circ$, identified by replicating our search using the photometric catalogue of the Hyper Suprime-Cam Subaru Strategic Program Public Release. Finally, we present the discovery of sixteen (*Yasone-5* to *Yasone-20*) new hypercompact cluster candidates in the Galactic disc. We discuss the possibility that any of the *Yasone* clusters may host an intermediate-mass black hole, and we advocate for follow-up spectroscopic observations to further constrain their nature.

Key words: methods: observational – techniques: photometric – catalogues – proper motions – galaxies: clusters: general – black hole physics

1 INTRODUCTION

Hypercompact stellar clusters (HCCs) are extremely dense, compact groups of stars characterized by sizes of ~ 1 pc and predicted to have large velocity dispersions often exceeding tens of km s^{-1} (Merritt et al. 2009; O’Leary & Loeb 2009). Proposed to host intermediate-mass black holes (IMBHs; with BH masses $\sim 100 - 10^6 M_\odot$ e.g., Mezcua 2017; Greene et al. 2020), HCCs are valuable theoretical laboratories for several reasons. These include: (i) investigating the initial conditions of star cluster formation (Lada & Lada 2003; Offner et al. 2014); (ii) studying the impact of stellar feedback on early dynamical evolution (Krumholz 2014; Dale 2015); (iii) examining the environmental regulation of star formation efficiency on small scales (Evans et al. 2009; Chevance et al. 2020); and (iv) probing massive BH astrophysics, including BH ejection and recoil dynamics (Spinosa et al. 2023; Izquierdo-Villalba et al. 2024), seed BH merging

history (Mezcua 2019; Untzaga et al. 2024), and the formation and detection of off-nuclear IMBHs (Barrows et al. 2019; Mezcua & Domínguez Sánchez 2024, 2025).

One possible mechanism to explain the presence of IMBHs in the outskirts of galaxies—often described as wandering black holes (WBHs)—is hierarchical merging. In the standard cosmological picture, galaxies grow mainly through the accretion and merging of smaller systems (e.g., Cole et al. 2000). Many of these systems, especially those at the massive end (i.e., satellites with stellar masses $\gtrsim 10^8 M_\odot$, higher than typical low-mass satellites), may host $\sim 10^3 - 10^4 M_\odot$ central IMBHs formed within their dense nuclear regions (e.g., Di Matteo et al. 2023; Izquierdo-Villalba et al. 2023). As such satellites merge with larger host galaxies, tidal forces can strip away their outer stellar envelopes until the only structure remaining is a compact stellar cluster bound to the satellite’s central IMBH. These compact remnants correspond to HCCs, and are usually retained by the gravitational sphere of influence of IMBHs of mass comparable to their own. Over time, however, stellar dynamical processes like two-

*E-mail: juntzaga96@gmail.com

body relaxation can erode the stellar component of HCCs (Merritt et al. 2009). N-body simulations suggest that the HCCs’ stellar mass may drop to $\sim 20\%$ of the IMBH mass over time, as stars are gradually lost to the new host galaxy via relaxation-driven evaporation (O’Leary & Loeb 2012; Rashkov & Madau 2013). In this framework, because these HCCs are low-mass in terms of stellar content, their dynamical friction timescales for sinking toward the centres of their new host galaxies can exceed several Gyr. Consequently, most HCCs observed today are expected to be long-lived remnants of past accretion events in their parent systems. By extension, the same reasoning applies to our own Galaxy: any HCCs that may be detected in the Milky Way (MW) would also have been subject to long sinking timescales, implying that they are likely relics of accretion episodes that occurred during the MW’s early formation stages (Greene et al. 2021; Weller et al. 2022).

IMBH formation can also occur *in situ*, within the MW itself, through a runaway merger scenario, potentially allowing for a more recent origin and a younger HCC population (Mapelli 2016; Rizzuto et al. 2021; Fujii et al. 2024; Reinoso et al. 2025). In this scenario, massive stars in an HCC can undergo mass segregation and concentrate at the core, where frequent dynamical interactions and collisions would lead to successive mergers, forming a single massive object that may eventually collapse into an IMBH. Alternatively, the assembly of IMBHs can be catalyzed by repeated mergers of stellar-mass BHs over time (see Zwart & McMillan 1999; Gaburov et al. 2008; Giersz et al. 2015; Mapelli 2016; Fragione 2022; Prieto et al. 2022; Ter-Kazarian 2022).

Alternative origin scenarios for HCCs are ultra-faint dwarf galaxies (UFDs) and compact globular clusters (GCs), particularly in the MW halo. UFDs are characterized by extremely low luminosities ($M_V \gtrsim -8$) and stellar masses below $10^5 M_\odot$, fainter than many classical GCs but structurally more extended, with typical half-light radii (r_h) in the range of ~ 20 –200 pc (Simon 2019; Ahvazi et al. 2024). Despite their low stellar masses, UFDs are dynamically dominated by dark matter (DM), exhibiting mass-to-light ratios that can exceed several hundred. Structurally and dynamically, they are distinct from both GCs and brighter dwarf spheroidal galaxies, though their integrated photometric properties —such as size and total luminosity— can partially overlap with those of faint GCs¹. This overlap has led to discussions about a possible misclassification of compact stellar systems, where, in the absence of spectroscopic confirmation of a DM halo, distinguishing a UFD from a diffuse GC can be challenging (e.g., Willman & Strader 2012). Some scenarios propose that the smallest and faintest UFDs may be the tidally stripped remnants of larger systems, including nucleated dwarfs, or the products of early accretion events during the hierarchical assembly of the MW (Bullock & Boylan-Kolchin 2017; Errani et al. 2025). The most compact UFDs, especially those with elevated mass-to-light ratios and small sizes, could plausibly host central BHs, and would resemble in many respects the expected properties of HCCs.

The discovery of extremely faint and compact dwarf galaxies such as Willman 1 (Willman et al. 2005) and Segue 1 (Belokurov et al. 2007) nearly two decades ago pushed the observational limits of what constitutes a satellite galaxy of the MW. These systems, characterized by absolute magnitudes fainter than $M_V \sim -3$, r_h smaller than 30 pc, and heliocentric distances (d) within 40 kpc, blurred the boundary between dwarf galaxies and extended GCs. Since then, subsequent

surveys and discoveries have continued to refine and challenge these limits. For instance, Carina III, with $r_h \sim 30$ pc, $d \sim 20$ kpc, and $M_V = -2.4$, was initially difficult to classify, with no trace of RR Lyrae stars at the time of discovery (Torrealba et al. 2018). Similarly, Draco II/Laevens 4, with $d \sim 20$ kpc, $M_V = -2.9$, and $r_h = 19$ pc, exemplifies the challenges of distinguishing between extended GCs and faint dwarf galaxies in the absence of robust kinematic information (Laevens et al. 2015).

This frontier has been pushed further with the recent discovery of Ursa Major III, a MW satellite with properties that are unprecedented among known compact stellar systems (Smith et al. 2024; Errani et al. 2024). With $M_V = +2.2$, $r_h \sim 3$ pc, and a d of just ~ 10 kpc, Ursa Major III is smaller, fainter, and closer than even the faintest GCs, such as HSC-1 ($M_V = -0.20$, $r_h \sim 6$ pc, $d = 46$ kpc; Homma et al. 2019). Ursa Major III currently represents the closest known compact stellar system plausibly resembling a true HCC. Nonetheless, the observational limit for the size of these systems remains to be pushed even further into the ~ 1 pc or even sub-pc regime, where most genuine HCCs are predicted to reside.

Regardless of whether HCCs formed *in situ* near the Galactic centre or *ex situ* in a satellite galaxy that was accreted later, they would eventually orbit near the Galactic disc and pass through it. Repeated disc passages, coupled with angular momentum loss, might shrink their orbits to within a few kpc of the centre, leaving only the densest core intact (e.g., Vansevičius et al. 2009). These remnants would be distinguishable from ordinary open clusters by their extreme densities and the potential presence of a central IMBH. However, while most compact clusters in the Galactic disc span sizes of few pc —comparable to the regime expected for HCCs— they are also characterized by young stellar populations with solar to super solar metallicity and short heliocentric distances below kpc scales. Some exceptions exist, such as Arp-Madore 2, a relatively old star cluster (~ 5 Gyr), with a relatively low metallicity ($[Fe/H] \sim -0.5$), a half-mass radius of 2.3 pc, and located at $d \sim 9$ kpc (Lee 1997).

Several other studies have focused on searching for HCCs. O’Leary & Loeb (2012) used the Sloan Digital Sky Survey (SDSS) Data Release 7 to look for HCC candidates and identified 100 objects with photometric properties consistent with theoretical models. However, no follow-up confirmation has been performed on these candidates. More recently, Lena et al. (2020) used the transmission curves and synthetic spectra of simulated HCCs across several major surveys, namely the SDSS (Abazajian et al. 2009), the Kilo-Degree Survey (de Jong et al. 2015), the VISTA Kilo-degree Infrared Galaxy Survey (Edge et al. 2013), the Canada-France-Hawaii Telescope Legacy Survey (Gwyn 2012), the Panoramic Survey Telescope and Rapid Response System (Pan-STARRS) (Chambers et al. 2016), the Global Astrometric Interferometer for Astrophysics (*Gaia*) (Brown et al. 2018), the Next Generation Virgo Cluster Survey (Ferrarese et al. 2012), and the Two Micron All-Sky Survey (Skrutskie et al. 2006), and reported several candidate HCCs, though none have been securely confirmed to date.

Greene et al. (2021) used a combination of the *Gaia* Early Data Release 3 (Brown et al. 2021) and the Dark Energy Camera Legacy Survey data release 9 (Schlegel et al. 2021) to search for $15''$ spatial overdensities in over 9,000 deg 2 of sky, which fit the theorized projected size of a ~ 1 pc HCC located at ~ 50 kpc. Although no strong candidates were found in that study, the authors presented upper limits on the occupation fraction, BH mass, and typical size of potential host HCCs. Wu et al. (2024) used data from *Gaia* Early Data Release 3 and Large-Area Multi-Object Fiber Optic Spectroscopic Telescope Data Release 7 (Collaboration 2020), along with additional data from Pan-STARRS and SDSS, to probe over six million

¹ See Figure 2 in Marleau et al. (2024), available at https://www.aanda.org/articles/aa/full_html/2024/10/aa49617-24/F2.html, which compares the sizes and luminosities of GCs and UFDs.

sources in search of HCCs potentially hosting IMBHs. In this case, one extended source with a stellar spectrum was detected, signaling a potential HCC candidate in the MW. However, further analysis revealed that the stellar spectrum did not belong to that candidate. Taking this information into account, along with the faint absolute magnitude and image characteristics of the candidate, it was finally discarded as well.

In this work, we aim to detect and characterize a sample of HCC candidates by searching for (1) compact stellar overdensities whose (2) colour–magnitude diagrams (CMDs) follow a low-metallicity isochrone, and which (3) have coherent tangential motion according to *Gaia* data. In §2 we describe the catalogues and selection techniques employed in this work. In §3 we present our list of HCC candidates along with their photometric and kinematic properties. In §4, we discuss the possible nature of these systems, including the likelihood of them hosting an IMBH, and conclude by outlining future work to elucidate their true nature.

2 DATASET & HCC SELECTION

In this section, we outline the data selection criteria applied to the surveys used in our analysis (§ 2.1), followed by a description of the methodology employed to identify HCC candidates (§ 2.2). Finally, we detail the photometric follow-up observations conducted for three of the identified candidates (§ 2.3).

2.1 Surveys

The following is a brief overview of the astronomical surveys whose catalogues have been utilized in this study. Specifically, we make use of data from the Pan-STARRS Data Release 2, the Hyper Suprime-Cam Subaru Strategic Program (HSC-SSP) Public Data Release 3, and the *Gaia* Data Release 3.

2.1.1 Pan-STARRS data

Pan-STARRS is a wide-field imaging system developed and operated by the Institute for Astronomy at the University of Hawaii. The Pan-STARRS1 (PS1) survey is the first component of the system to be completed and forms the basis for both Data Releases 1 and 2. PS1 employs a 1.8 m telescope equipped with a 1.4-gigapixel camera to image approximately three-quarters of the sky (declinations between $+90^\circ$ and -30°) across five broadband filters (g, r, i, z, y), reaching limiting magnitudes of $grizy < 23.3, 23.2, 23.1, 22.3, 21.3$ (Chambers et al. 2018; Flewelling et al. 2020; Magnier et al. 2020a,b,c; Waters et al. 2020).

For this work, we select candidate halo stars by first applying a Galactic latitude cut of $|b| > 20^\circ$. This aims to preferentially select objects in the Galactic halo while avoiding the crowded stellar fields close to the Galactic plane, where overdensities are most often associated with young open clusters that neither trace past merger events nor are expected to host IMBHs. While a higher latitude cut would further reduce such contamination, we deliberately set the limit at $|b| = 20^\circ$ to maximize overlap with the sky coverage of the HSC-SSP database (see Figure 1), enabling a consistent crossmatch with this same sub-sample in later stages of the analysis. Then we perform a morphological filter requiring the variation between the mean point spread function magnitude and the mean Kron magnitude in the g , r , and i bands to be less than 0.05, following Tachibana & Miller (2018). As a sanity check, we additionally ensure that all selected

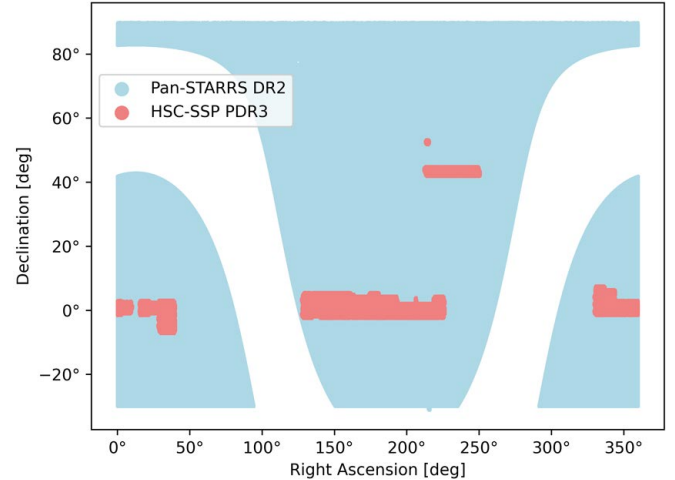


Figure 1. Sky map of the stars selected from the Pan-STARRS (blue) and HSC-SSP (red) surveys, shown in equatorial coordinates (RA–Dec). A galactic latitude cut of $|b| > 20^\circ$ is imposed to ensure all sources are located in the MW halo. The corresponding masked region—aligned with the Galactic plane—is clearly visible as the white band running across the map, despite the equatorial coordinate projection.

sources have valid magnitude measurements and consistent photometric uncertainties in the g , r , and i bands to minimize contamination from spurious detections and artifacts. Specifically, we remove duplicate detections, which are particularly common in regions where small systematic astrometric shifts ($\lesssim 0.5''$) cause the same source to appear multiple times. In these cases, we retain the entry with the highest number of contributing detections (`nDetections` in the PS1 database), as it most reliably represents the true source. We also exclude objects with excessively large or undefined magnitude uncertainties in any of the g , r , or i bands, as such values are indicative of poor photometry or image artifacts. These quality-control steps are implemented directly on the Pan-STARRS Data Release 2 catalog queries, using the `ps1_stack` table parameters to filter by `nDetections`, photometric flags, and error thresholds. After these cuts, the resulting sample contains approximately 150 million high-quality halo stars, spanning $\sim 65\%$ ($\sim 20,000 \text{ deg}^2$) of the full PS1 footprint (see Figure 1, blue region).

In addition, we create a secondary dataset using the same quality constraints but targeting a complementary region of the sky. For this dataset (which will be referred as *disc-associated* in further sections), we impose a Galactic latitude constraint of $|b| < 20^\circ$ and proceed to explore the whole region between declination $+90^\circ$ and $+10^\circ$, which corresponds approximately to $\sim 1.000 \text{ deg}^2$ of sky coverage. This low-latitude dataset allows us to look for stellar overdensities in regions closer to the Galactic plane, where crowding and extinction are more prominent but where HCC candidates may still be present.

2.1.2 HSC-SSP data

HSC-SSP is a wide-field multi-band imaging survey conducted with the 8.2 m Subaru Telescope, developed by the National Astronomical Observatory of Japan in collaboration with various international academic and industrial partners. The survey employs an 870-megapixel digital camera to observe a total sky area of $1,470 \text{ deg}^2$ across three different depths: Wide, Deep, and UltraDeep, with $grizy$ limiting magnitudes of ~ 26 , ~ 27 , and ~ 28 , respectively (Furusawa et al.

2018; Kawanomoto et al. 2018; Komiyama et al. 2018; Miyazaki et al. 2018; Aihara et al. 2022).

Since all data available already correspond to halo sources ($|b| > 20$), we make the selection by imposing a set of constraints for well-defined stars. The HSC database includes a type-classification variable for each object, representing the probability that a source is a star, galaxy, or quasi-stellar object (QSO). While probabilities for stellar and QSO classifications range continuously between 0 and 1, the galaxy/non-galaxy distinction is binary (with a flag of 0 for extragalactic and 1 for galactic sources). However, since $\sim 70\%$ of HSC sources lack a definitive classification, we implement the following procedure: (1) exclude all sources explicitly classified as galaxies, (2) retain sources with a stellar probability $p_{\text{star}} \geq 0.5$ (and hence $p_{\text{QSO}} < 0.5$), and (3) for sources with unknown classifications, require that they be identified as point sources in all of the g , r , and i bands.

As with the Pan-STARRS dataset, we ensure that all selected sources possess reliable magnitude values and consistent photometric uncertainties in the g , r , and i bands. To further minimize contamination from extended objects, we additionally reject any source that, despite being classified as a star, is morphologically extended in at least two out of the three main filters (g , r , i). Finally, for the small fraction of objects with associated spectroscopic measurements, we exclude any source with a redshift $z > 0.1$.

This filtering yields approximately 30 million well-defined halo stars across the entire HSC-SSP footprint (see Figure 1; red regions). While our Pan-STARRS stellar selection spans over ten times the sky area of HSC, the HSC dataset offers a stellar source density approximately three times higher, primarily due to its significantly deeper photometric limit.

2.1.3 *Gaia* data

Gaia is a European Space Agency mission designed to provide high-precision astrometry, photometry, and spectroscopy for both MW stars and extragalactic sources. *Gaia* Data Release 3 includes measurements of stellar positions, parallaxes, proper motions, radial velocities, and brightness, enabling the construction of an accurate three-dimensional map of the Galaxy (Prusti et al. 2016; Hodgkin et al. 2021; Vallenari et al. 2022). Although *Gaia* Data Release 3 contains the sky regions surveyed by Pan-STARRS and HSC-SSP, its relatively bright limiting magnitude ($G \sim 21$) means that only the brighter fraction of stars in our candidate overdensities have counterparts in the *Gaia* catalogue.

2.2 Candidate Selection

We look for HCC candidates in the selected (see § 2.1) data by running a cluster-finding algorithm that identifies statistically significant overdensities relative to the local stellar background. We then perform a thorough examination in colour-magnitude space of each overdensity, fitting its stars to evolutionary tracks of synthetic populations of isochrone stars generated from the MESA² Isochrones and Stellar Tracks (MIST) models (Paxton et al. 2010, 2013, 2015; Choi et al. 2016; Dotter 2016). As a final step, overdensities with well-fitted isochrone structures are then cross-matched with the *Gaia* Data Release 3 catalogue in order to ensure that they have coherent proper motions as well.

² Modules for Experiments in Stellar Astrophysics, see <https://waps.cfa.harvard.edu/MIST/index.html>.

2.2.1 Finding overdensities

The data refinement starts by removing any duplicates. We identify any group of sources that have a separation $<1''$ in the case of Pan-STARRS and $<0.5''$ in the case of HSC-SSP and remove all candidates except for the ones with the highest number of detection counts (nDetections in the surveys' notation). We then proceed to cross-match our data with the NASA/IPAC Extragalactic Database and the Set of Identifications, Measurements and Bibliography for Astronomical Data in order to remove all known GCs, open clusters and low-redshift galaxies.

To mitigate contamination from stars with photometric measurements near the instrumental detection limit (where uncertainties are high and colour information is unreliable) we apply a provisional magnitude cut: $g < 21$ for Pan-STARRS and $g < 25$ for HSC-SSP (see Figure 2). This ensures that candidate overdensities are primarily composed of stars bright enough to plausibly trace the main-sequence turn-off of a synthetic isochrone population up to ~ 50 kpc. These sources are also more likely to have counterparts in the *Gaia* database, facilitating subsequent kinematic confirmation of their nature as compact clusters. Following this, we perform a two-dimensional (right ascension and declination) clustering search of the selected data from Pan-STARRS and HSC-SSP using a KDTree algorithm. Our code registers all the stellar neighbours of each star within a certain 2D distance that we set at $15''$, emulating the theorized projected size of a ~ 1 pc HCC located at ~ 50 kpc (see Greene et al. 2021).

In the HSC-SSP dataset, we find 67 overdensities with 11 stars, 27 overdensities with 12 stars, 17 overdensities with 13 stars, 8 overdensities with 14 stars, and 3 overdensities with 15 stars. In the halo-defined Pan-STARRS dataset ($|b| > 20$), we find 214 overdensities with 10 stars, 40 overdensities with 11 stars, and 6 overdensities with 12 stars. In the disc-associated Pan-STARRS dataset, we find 245 overdensities with highly varying stellar counts ranging from fewer than 10 to more than 30, depending on declination.

All identified overdensities are located at a minimum angular separation of $1'$ from any known object, and each is flagged as a statistically significant density outlier. To quantify this, we generate two hundred mock regions of $15''$ radius distributed randomly within a $3'$ background area around each overdensity. We then compare the stellar counts contained in each mock region with the ones spotted in the detected overdensity. Only those overdensities that exceed the local background density by more than 4σ are retained for further analysis.

2.2.2 CMD fitting

For each candidate overdensity, we expand the search radius up to $40''$ to ensure that no potential member stars of the HCC are excluded. We then assess the stellar populations of these overdensities using CMDs in both g vs. $(g - r)$ and r vs. $(r - i)$ spaces. The CMDs are compared against a suite of synthetic isochrones generated from MIST.

We generate isochrones covering a wide range of ages ($5 \leq \log(\text{age}[{\text{yr}}]) \leq 10.3$) and metallicities ($-4 \leq [\text{Fe}/\text{H}] \leq +0.5$) and overlay them on the CMDs of each overdensity. Two free parameters—total extinction $A(V)$ and heliocentric distance—are varied to identify the best-fitting configuration for each candidate. The best-fit isochrone is defined as the one that maximizes the number of stars aligned with the colour-magnitude locus of the main sequence predicted by the isochrone model, thereby providing the most consistent match with the observed stellar population. Once this isochrone is de-

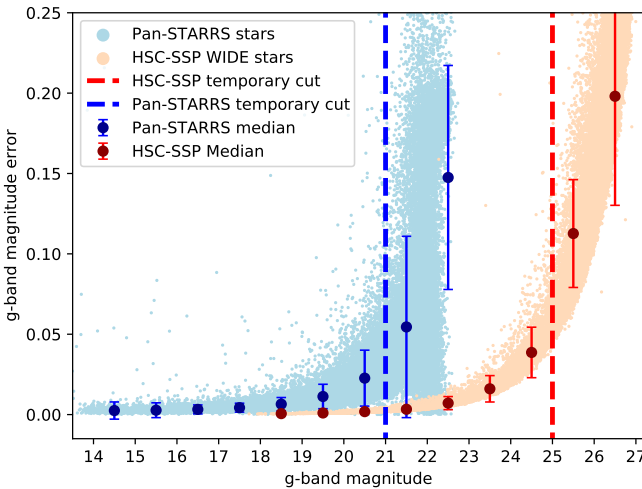


Figure 2. Magnitude values in the g -band of two samples of 50,000 stars from Pan-STARRS (light blue) and HSC-SSP (light red) in function of their respective magnitude errors. The points indicate the median of the magnitude errors for both Pan-STARRS (blue) and HSC-SSP (red). The dashed lines show the temporary cut performed in Pan-STARRS (blue) and HSC-SSP (red) in order to avoid the over-representation of high-error sources in our overdensities.

terminated, we remove all stars that lie beyond 1σ from the isochrone locus in both colour spaces. Additionally, we discard any overdensity in which fewer than half of its stellar members are consistent with the best-fitting isochrone. As a further sanity check, we attempt to fit the $3'$ surrounding stellar background using the same isochrone parameters derived for the overdensity. To do this, we select several annular regions around each candidate —each with an area equal to that of the overdensity— and examine the behaviour of the background stars in the CMD. For each annular region, we plot the number of field stars aligned with the isochrone and compare it with the number of isochrone matches obtained for the overdensity. Only overdensities that represent $>4\sigma$ outliers are considered for subsequent analysis. After applying these selection criteria, from the HSC-SSP dataset we are left with 6 overdensities; and from the two Pan-STARRS datasets we are left with 44 halo-associated overdensities and 19 disc-associated overdensities.

2.2.3 Gaia cross-matching

We utilize the *Gaia* database to provide kinematic confirmation of the cluster nature of our overdensities by cross-matching their bright-end stellar members and searching for clumps in proper motion space. Due to the depth limitations of *Gaia* (with a typical detection threshold of $G \sim 21$), approximately 40% of stars from Pan-STARRS-selected overdensities lack a *Gaia* counterpart. In the case of HSC-SSP, this fraction increases to 85%, making it especially challenging to confirm HSC-selected overdensities via kinematics.

To identify potential cluster members in proper motion space, we search for overdensities of sources within circular regions of 0.5 to 1 mas yr^{-1} radius. These regions are considered significant when they appear as isolated clumps in proper motion space, distinct from the background distribution of stars located within $3'$ of the candidate centroid. As an additional consistency check, we compute the pairwise distances in proper motion space between all stars within $3'$ of each candidate, and compare the resulting distribution to the pairwise distances among the candidate's stellar members. Candidates

are retained only if their bright-end stellar members constitute a $> 4\sigma$ kinematic overdensity relative to the surrounding field population in proper motion space.

After applying these criteria, we are left with three halo candidates from the Pan-STARRS database (*Yasone-1*, *Yasone-2*, and *Yasone-3*). We also retain one candidate from the HSC-SSP data (*Yasone-4*), although its nature remains uncertain due to the faintness of its member stars, which prevents further analysis. Finally, we identify 16 additional compact clusters in the disc-associated Pan-STARRS dataset (*Yasone-5* through *Yasone-20*). The coordinates and main properties of these HCC candidates are presented in Table 2.

2.3 Follow-up observations

We use the Gran Telescopio CANARIAS Optical System for Imaging and low-Intermediate-Resolution Integrated Spectroscopy (GTC OSIRIS) in broadband imaging mode (see [Cepa 1998](#); [Cepa et al. 2000, 2003](#)). It provides a field of view of $7.8' \times 8.5'$ ($7.8' \times 7.8'$ unvignetted) while covering the full spectral range from $\lambda=3650\text{\AA}$ to $\lambda=10000\text{\AA}$. The instrument uses SDSS broadband filters u' , g' , r' , i' , z' and features a high transmission efficiency, especially at longer wavelengths. OSIRIS also supports charge-shuffling mode and is equipped with a red-sensitive 2048×4096 Marconi CCD42-82 detector, making it ideal for deep follow-up optical imaging observations.

We make use of GTC OSIRIS to obtain deep broad-band imaging in order to confirm the physical nature of our three halo-associated stellar overdensities (*Yasone-1*, *Yasone-2*, and *Yasone-3*), initially identified through a combination of Pan-STARRS and *Gaia* datasets. Due to the limiting magnitudes of Pan-STARRS and *Gaia*, we were only able to trace the upper red-giant branch (RGB) structures of these candidates, with little to no constraint on their main sequence or main sequence turn-off regions. To probe these critical evolutionary phases, deeper imaging was required to reach magnitudes of at least g , r , $i \approx 25.0$ with a signal-to-noise ratio greater than 10 across all bands.

A total of nine hours of observing time were awarded, scheduled in nine blocks of approximately 54 minutes each, alternating between the g , r , and i filters, with intervals allocated for telescope repositioning and to avoid CCD saturation (see Table 1). The first three hours of observations were carried out on July 8th, 2023, targeting the *Yasone-1* candidate. These observations were conducted under cloudless, dark-moon conditions, with a seeing ranging between $0.8''$ and $1.1''$ during the first hour. Subsequent exposures were progressively affected by internal reflections from bright stars and the rising moon. *Yasone-2* was observed on the night of July 9th, 2023, under similarly cloudless but grey-moon conditions, achieving a seeing of $\sim 0.6''$ for most of the session. The *Yasone-3* candidate was observed over two nights: July 23rd, during which some frames were degraded by short-term oscillations, and August 16th, where a few exposures were affected by satellite trails and seeing exceeding the $1.2''$ threshold. Despite these minor limitations, the overall quality of the retrieved data was satisfactory, and the data reduction was performed utilizing the SAUSERO³ software ([Pérez-Toledo 2025](#)). In all three fields, the deeper imaging allowed the identification of new and faint stellar members consistent with the expected cluster populations. When displayed in colour-magnitude space alongside the RGB sources from Pan-STARRS, we applied the filter transformations from [Tonry et al. \(2012\)](#).

³ Software to AUomatize in a Simple Environment the Reduction of Osiris+ data.

Table 1. Summary of GTC/OSIRIS observations for the *Yasone* targets

ID	Date (UTC)	Target	R.A. (J2000) (hh:mm:ss)	Dec. (J2000) (dd:mm:ss)	Obs. Time (min)	Seeing (arcsec)	Clouds	Moon	Notes
0001	2023-07-08	<i>Yasone-1</i>	17:42:04.85	+13:10:17.3	47.5	0.8–1.1	Clear	Dark	Nothing remarkable
0002	2023-07-08	<i>Yasone-1</i>	17:42:04.85	+13:10:17.3	47.5	0.6–1.0	Clear	Bright	Reflection in some <i>r</i> -band frames
0003	2023-07-08	<i>Yasone-1</i>	17:42:04.85	+13:10:17.3	47.5	0.7–0.9	Clear	Bright	Moonrise near end of observation
0004	2023-07-09	<i>Yasone-2</i>	17:29:23.81	+06:25:22.9	47.5	0.6–0.7	Clear	Dark	Nothing remarkable
0005	2023-07-09	<i>Yasone-2</i>	17:29:23.81	+06:25:22.9	47.5	~0.6	Clear	Grey	System error during <i>r</i> -band acquisition
0006	2023-07-09	<i>Yasone-2</i>	17:29:23.81	+06:25:22.9	47.5	~0.6	Clear	Grey	Nothing remarkable
0007	2023-07-23	<i>Yasone-3</i>	19:31:51.02	-26:26:59.8	47.5	~0.9	Clear	Dark	Oscillations, extra image taken
0008	2023-08-16	<i>Yasone-3</i>	19:31:51.02	-26:26:59.8	47.5	0.8–1.2	Clear	Dark	Satellite trail, extra image taken
0009	2023-08-16	<i>Yasone-3</i>	19:31:51.02	-26:26:59.8	47.5	0.8–1.2	Clear	Dark	Nothing remarkable

3 RESULTS

In this section we present the *Yasone* catalogue, our list of newly discovered HCC candidates obtained after following the procedure described in the previous section. Table 2 provides the most relevant information of each candidate, including astrometric, photometric, and structural parameters. In §3.1 we focus the analysis on our candidates located in the halo regions of the sky (*Yasone-1* to *Yasone-4*, both included), complementing kinematic and photometric data from the *Gaia* and Pan-STARRS database respectively, with deep photometric observations from GTC. In §3.2 we present sixteen additional candidates (*Yasone-5* to *Yasone-20*, both included) with locations closer to the Galactic plane.

3.1 Halo Candidates

We identify four HCC candidates in the Galactic halo. *Yasone-1*, *Yasone-2*, and *Yasone-3* were discovered by combining Pan-STARRS, *Gaia*, and deep *gri* imaging from GTC/OSIRIS. These lie at similar vertical distances from the Galactic plane ($|b| \sim 20^\circ$; Figure 3). *Yasone-4* was identified with Pan-STARRS, *Gaia*, and deeper HSC Subaru data, enabling its detection at a higher latitude ($b \sim 48^\circ$; Figure 3). *Yasone-4* is smaller and fainter than the other candidates (Figure 4; bottom filled magenta hexagon), and due to limited GTC/OSIRIS time, no follow-up is available.

All four candidates exhibit small angular sizes, with half-light radii of $r_h \sim 25''$ (see Figure 4), and faint apparent magnitudes exceeding 16 mag. Nevertheless, each was identified as a statistically significant overdensity, standing out as a $> 4\sigma$ deviation above the local control field. For *Yasone-1*, *Yasone-2*, and *Yasone-3*, follow-up photometry from GTC confirms their nature as stellar overdensities (see Figure 5), with the total angular size of each candidate being estimated approximately at 40 arcseconds. Additionally, Figures 6, 7, and 8 show the photometric analyses of candidates *Yasone-1*, *Yasone-2*, and *Yasone-3*, respectively.

3.1.1 *Yasone-1*

Deep GTC imaging of *Yasone-1* reveals 29 *g*-band and 34 *r*-band point-like sources with magnitudes ~ 22 –27 within $40''$ of its centroid, comprising 42 unique stellar members in total (see Table 2, fifth column). Due to differences in depth and detection efficiency, not all sources are detected in both filters. For those sources with

reliable detections in both the *g*- and *r*-bands, we apply a stricter selection, retaining only those that trace the isochrone-defined main sequence consistently in both $g - r$ and $r - i$ colours. For sources detected in only one band, we still require their photometry to be broadly consistent with the isochrone in the corresponding colour-magnitude space, though these cases naturally appear in only one of the CMD panels. This filtering explains the unequal number of stellar sources visible in the central top and bottom panels of Figure 6. We also identify one additional Pan-STARRS source with consistent colour behaviour in $g - r$ and $r - i$, although it is too faint to appear in *Gaia* and thus lacks kinematic confirmation.

As a sanity check, we define an annular background region surrounding the candidate, with an inner radius twice that of the cluster and an equal projected area. When overplotted on the same isochrone, this control field does not trace a coherent main sequence (Figure 6, right panels). This result is consistent across several background annuli with varying radii. Notably, none of the sources in these background regions simultaneously falls within both the kinematic selection area (Figure 9, left panel) and the isochrone-defined main sequence. We try multiple isochrone configurations to the *Yasone-1* candidate and find the best fit to be that of an old (12^{+1}_{-2} Gyr), metal-poor ($[\text{Fe}/\text{H}] = -1.5 \pm 0.25$) stellar population at a heliocentric distance of 12^{+3}_{-2} kpc⁴ (although the absence of spectroscopic data makes these values tentative). With this heliocentric distance, we estimate an absolute magnitude⁵ of $2.10^{+0.40}_{-0.48}$ in the *g*-band and $+2.36^{+0.40}_{-0.48}$ in the *V*-band, a total stellar mass⁶ of $18.2^{+10.2}_{-5.6} \text{ M}_\odot$ (assuming a stellar mass-to-light ratio in the *g*-band of 1.09), and a

⁴ The quoted uncertainties in age, metallicity, and heliocentric distance reflect the range of isochrone parameters that provide acceptable fits (within ~ 0.1 mag in colour-magnitude space) to the cluster's stellar population.

⁵ To compute absolute magnitudes, we first calculate the distance modulus as $5 \log_{10}(d/10 \text{ pc})$, subtract it from the observed apparent magnitudes, and then convert to luminosities in solar units using $M_{\odot,g} = 5.16$ and $M_{\odot,V} = 4.83$ from Willmer (2018). The transformation from *g*-band to *V*-band magnitudes was performed following Tonry et al. (2012). The associated uncertainties reflect the propagated errors from the lower and upper bounds of the adopted heliocentric distance.

⁶ To estimate the total stellar mass, we first compute individual absolute magnitudes and sum their luminosities in solar units, adopting $M_{\odot,g} = 5.16$. We then apply a colour-based mass-to-light ratio in the *g*-band derived from the mean ($g - r$) colour using the relation $\log_{10}(M/L_g) = 1.774(g - r) - 0.783$ from Into & Portinari (2013).

Table 2. The *Yasone* catalog of newly discovered hyper-compact cluster candidates presented in this work

ID	R.A. (J2000) (deg) (1)	Dec. (J2000) (deg) (3)	Data (4)	N (5)	$r_h^{(a)}$ ($''$) (6)	A_V (mag) (7)	Age ^(b) (Gyr) (8)	$d^{(b)}$ (kpc) (9)	$R^{(c)}$ (kpc) (10)	[Fe/H] ^(b) (11)	σ_{pm} (mas yr $^{-1}$) (12)	m_g (mag) (13)
Halo												
<i>Yasone-1</i>	265.52019	13.17146	<i>Gaia</i> + PS1 + GTC	42	24	1.0	12^{+1}_{-2}	12^{+3}_{-2}	8^{+2}_{-1}	-1.5 ± 0.25	0.10	16.5
<i>Yasone-2</i>	262.34921	6.42302	<i>Gaia</i> + PS1 + GTC	45	25	0.8	12^{+1}_{-2}	20^{+10}_{-12}	14^{+10}_{-9}	-1.5 ± 0.25	0.62	16.3
<i>Yasone-3</i>	292.96258	-26.44994	<i>Gaia</i> + PS1 + GTC	51	29	1.0	12^{+1}_{-2}	15^{+3}_{-5}	8^{+3}_{-4}	-2.0 ± 0.25	—	16.5
<i>Yasone-4^(d)</i>	225.68761	-0.91947	<i>Gaia</i> + PS1 + HSC	15	23	—	—	—	—	—	—	18.4
Disc												
<i>Yasone-5</i>	95.88220	20.76780	<i>Gaia</i> + PS1	34	24	2.4	$0.3^{+0.7}_{-0.2}$	$13.5^{+0.5}_{-2.0}$	$21.6^{+0.5}_{-2.0}$	0.0 ± 0.25	0.32	14.9
<i>Yasone-6</i>	93.99560	10.87850	<i>Gaia</i> + PS1	24	20	2.2	$1.0^{+2.0}_{-0.7}$	$6.0^{+0.5}_{-2.5}$	$14.0^{+0.5}_{-2.4}$	0.0 ± 0.25	0.26	15.4
<i>Yasone-7</i>	12.42938	70.43137	<i>Gaia</i> + PS1	13	24	2.0	$1.0^{+2.0}_{-0.7}$	$7.0^{+0.5}_{-0.5}$	$13.3^{+0.4}_{-0.4}$	0.5 ± 0.25	0.17	15.8
<i>Yasone-8</i>	330.78870	60.75680	<i>Gaia</i> + PS1	18	17	2.5	$1.0^{+2.0}_{-0.7}$	$7.0^{+3.0}_{-2.0}$	$12.0^{+2.4}_{-1.4}$	0.0 ± 0.25	0.64	16.4
<i>Yasone-9</i>	316.50120	45.98940	<i>Gaia</i> + PS1	41	22	2.8	$0.3^{+0.7}_{-0.2}$	$8.5^{+3.5}_{-2.5}$	$11.5^{+2.7}_{-1.6}$	0.0 ± 0.25	0.47	15.0
<i>Yasone-10</i>	302.37750	40.73327	<i>Gaia</i> + PS1	23	12	2.4	$1.0^{+2.0}_{-0.7}$	$10.0^{+2.0}_{-1.0}$	$11.4^{+1.5}_{-0.7}$	0.5 ± 0.25	0.47	16.6
<i>Yasone-11</i>	298.09783	29.94878	<i>Gaia</i> + PS1	32	13	1.8	$1.0^{+2.0}_{-0.9}$	$1.0^{+0.5}_{-0.5}$	$7.8^{+0.1}_{-0.2}$	0.0 ± 0.25	0.63	15.7
<i>Yasone-12</i>	295.19450	30.15050	<i>Gaia</i> + PS1	61	28	2.2	$1.0^{+2.0}_{-0.7}$	$6.0^{+1.5}_{-0.5}$	$7.9^{+0.6}_{-0.1}$	0.0 ± 0.25	0.52	15.3
<i>Yasone-13</i>	338.52182	57.71902	<i>Gaia</i> + PS1	25	15	2.2	$3.0^{+2.0}_{-2.0}$	$4.0^{+1.0}_{-1.5}$	$10.0^{+0.6}_{-0.8}$	0.0 ± 0.25	0.65	15.6
<i>Yasone-14</i>	302.60948	40.92500	<i>Gaia</i> + PS1	36	15	2.7	$0.3^{+0.7}_{-0.2}$	$15.0^{+2.0}_{-2.0}$	$15.5^{+1.7}_{-1.7}$	0.0 ± 0.25	0.54	15.8
<i>Yasone-15</i>	100.54790	11.73720	<i>Gaia</i> + PS1	26	23	2.7	$1.0^{+2.0}_{-0.7}$	$7.0^{+1.0}_{-1.5}$	$14.9^{+1.0}_{-1.5}$	0.0 ± 0.25	0.45	15.5
<i>Yasone-16</i>	327.23950	59.01930	<i>Gaia</i> + PS1	37	22	2.3	$1.0^{+1.0}_{-0.7}$	$6.0^{+2.5}_{-2.0}$	$11.0^{+1.8}_{-1.3}$	0.0 ± 0.5	0.60	15.6
<i>Yasone-17</i>	331.34584	55.14620	<i>Gaia</i> + PS1	25	14	2.2	$1.0^{+2.0}_{-0.7}$	$6.0^{+3.0}_{-1.5}$	$11.0^{+2.2}_{-1.0}$	0.0 ± 0.25	0.56	16.3
<i>Yasone-18</i>	316.83027	45.91032	<i>Gaia</i> + PS1	24	13	2.6	$0.3^{+0.7}_{-0.2}$	$8.0^{+3.0}_{-1.5}$	$11.2^{+2.2}_{-1.0}$	0.0 ± 0.25	0.54	15.7
<i>Yasone-19</i>	298.82535	35.49282	<i>Gaia</i> + PS1	22	11	2.7	$1.0^{+2.0}_{-0.7}$	$5.0^{+1.5}_{-2.0}$	$8.1^{+0.6}_{-0.3}$	0.0 ± 0.5	0.49	15.7
<i>Yasone-20</i>	296.25171	16.28925	<i>Gaia</i> + PS1	25	10	2.0	$1.0^{+2.0}_{-0.7}$	$8.0^{+1.5}_{-2.0}$	$7.3^{+0.8}_{-0.6}$	0.0 ± 0.25	0.34	15.7

Columns. (1) Candidate name within the *Yasone* catalogue, (2) right ascension, (3) declination, (4) surveys, catalogues and/or photometric observations used in the study of the candidate, (5) number of stellar members, (6) half-light radius, (7) line-of-sight extinction, (8) age, (9) heliocentric distance, (10) galactocentric distance, (11) metallicity, (12) proper motion dispersion, (13) apparent magnitude in the g-band.

^aThroughout this work, half-light radius is defined as the distance from the centroid enclosing half the stellar members, not half the surface brightness. (See [Martin et al. 2008](#) for a review on how to compute r_h for cluster-like objects with a small angular size).

^bThese values have been often derived from the isochrone fitting of very limited photometric data and are subjected to significant errors.

^cThe galactocentric distances are computed using the heliocentric distances and assuming a distance from the Sun to the Galactic centre of $R_0 = 8178$ pc ([Abuter et al. 2019](#)) and a height above Galactic plane of $z_\odot = 17.1$ pc ([Karim & Mamajek 2016](#)).

^d*Yasone-4* is a low-confidence candidate; sparse, faint sources preclude robust confirmation of its cluster nature.

physical r_h of $1.40^{+0.35}_{-0.23}$ pc⁷ (see Figure 4, bottom panel). However, it is important to note that the stellar mass estimate represents a lower limit as it is only derived from the observed stellar sources. The deep photometric imaging obtained for our candidates reaches sources as faint as $g \sim 26.5$, corresponding to a main sequence stellar mass of $\sim 0.23 M_\odot$ at the estimated heliocentric distance of 12 kpc. We do not know the true underlying stellar mass function, but if we assume it roughly follows a Kroupa ([Kroupa 2001](#)) initial mass function, then we estimate that we have directly observed 73% of the total stellar mass in the system. We have not observed every star, but we have captured a significant fraction of the stellar mass currently present.

⁷ The uncertainties associated with r_h reflect the propagated errors from the lower and upper bounds of the adopted heliocentric distance.

Additionally, we identify three *Gaia* sources within $40''$ of the candidate's centroid (Figure 6, left panels) that align with a red giant branch-like structure in both $g - r$ and $r - i$ when overplotted with a representative isochrone (Figure 6, centre panels). These stars are also part of a kinematic overdensity in proper motion space (Figure 9, left panel). Notice however, that the data used in the CMDs corresponding to bright stars doesn't actually belong to the *Gaia* database; it belongs to the Pan-STARRS database after crossmatching with *Gaia* and applying a cut based on the proper motion values of the sources (see §2). We are only using the *Gaia* database directly in the proper motion plots shown in Figure 9.

Finally, *Gaia*'s astrometric data of *Yasone-1*'s three brightest stellar members yield the following mean proper motion: $\mu_\alpha \cos \delta = -3.63$ mas yr $^{-1}$, $\mu_\delta = -3.70$ mas yr $^{-1}$, and total proper motion $\mu = 5.18$ mas yr $^{-1}$, with a proper motion dispersion of

$\sigma_{\text{pm}} = 0.10 \text{ mas yr}^{-1}$ (Figure 9, left panel). Applying our heliocentric distance estimation, we obtain tentative kinematic values: $v_\alpha \cos \delta = -206_{-52}^{+34} \text{ km s}^{-1}$, $v_\delta = -211_{-53}^{+35} \text{ km s}^{-1}$, a total heliocentric tangential velocity $v_{\text{tan}} = 295_{-49}^{+74} \text{ km s}^{-1}$, and an associated velocity dispersion of $\sigma_v = 5.89_{-0.98}^{+1.47} \text{ km s}^{-1}$. Notice that the velocity dispersion measurements of our candidates are upper limits. The *Gaia* uncertainties in proper motion space appear to be larger than those formally stated, which contributes to some of the measured velocity dispersion (e.g., see Vasiliev & Baumgardt 2021).

3.1.2 *Yasone-2*

Deep GTC imaging of *Yasone-2* reveals 37 *g*-band and 40 *r*-band point-like sources with magnitudes $\sim 22\text{--}27$ within $40''$ of its centroid, comprising 45 unique stellar members in total (see Table 2, fifth column). Additionally, we identify two Pan-STARRS sources with consistent colour behaviour in *g* – *r* and *r* – *i* but no *Gaia* counterpart. When performing isochrone fitting on the control field, we observe a slightly better colour-structure compared to *Yasone-1*, but still far from that of the candidate’s (see Figure 7, right panels).

We find the best fit for *Yasone-2* to be that of an old (12_{-2}^{+1} Gyr), metal-poor ($[\text{Fe}/\text{H}] = -1.5 \pm 0.25$) stellar population at a heliocentric distance of 20_{-12}^{+10} kpc. With this tentative heliocentric distance we can estimate $M_g = 1.62_{-0.88}^{+1.99}$, $M_V = +1.83_{-0.88}^{+1.99}$, a total stellar mass of $28.0_{-23.5}^{+35.0} M_\odot$ (assuming a mass-to-light ratio in the *g*-band of 1.08) and $r_h = 2.44_{-1.46}^{+1.22} \text{ pc}$ (see Figure 4, bottom). The lowest mass star observed at the heliocentric distance of 20 kpc is $\sim 0.35 M_\odot$, implying we have observed roughly 53% of the total stellar mass in *Yasone-2* (under the assumption of a Kroupa IMF).

We also identify four *Gaia* sources within $40''$ of the candidate’s centroid (Figure 7, left panels) that align with a RGB-like structure in both *g* – *r* and *r* – *i* (Figure 7, centre panels) and are also part of a kinematic overdensity in proper motion space (Figure 9, centre panel). None of the background sources has a good match in colour-magnitude space and proper motion space simultaneously (Figure 9, centre panel). The four *Gaia* sources yield the following mean proper motion: $\mu_\alpha \cos \delta = -1.04 \text{ mas yr}^{-1}$, $\mu_\delta = -2.38 \text{ mas yr}^{-1}$, and total proper motion $\mu = 2.59 \text{ mas yr}^{-1}$, with a proper motion dispersion of $\sigma_{\text{pm}} = 0.62 \text{ mas yr}^{-1}$, which can be lowered to 0.40 mas yr^{-1} if we were to exclude the source with the highest associated error and slightly displaced proper motion coordinates with respect to the other three (Figure 9, centre panel). Applying our distance estimation, we obtain kinematic values: $v_\alpha \cos \delta = -99_{-49}^{+59} \text{ km s}^{-1}$, $v_\delta = -225_{-113}^{+135} \text{ km s}^{-1}$, a total heliocentric tangential velocity $v_{\text{tan}} = 246_{-148}^{+123} \text{ km s}^{-1}$, and an associated velocity dispersion of $\sigma_v = 59_{-35}^{+30} \text{ km s}^{-1}$, which can be lowered to $\sigma_v = 38_{-23}^{+19} \text{ km s}^{-1}$ if subtracting the source with largest error.

3.1.3 *Yasone-3*

Deep GTC imaging of *Yasone-3* reveals 39 *g*-band and 33 *r*-band point-like sources with magnitudes $\sim 22\text{--}27$ within $40''$ of its centroid, comprising 51 unique stellar members in total (see Table 2, fifth column). Additionally, we identify two Pan-STARRS sources with consistent colour but no *Gaia* counterpart. Although the candidate displays a significantly higher stellar density compared to the control field (which also shows an absence of colour structure, see Figure 8, right panels) the spatial distribution of *Yasone-3* is slightly more dispersed than the other two candidates, resulting in a larger r_h . Nevertheless, all three of them share the fact that no field sources match

in colour-magnitude space and proper motion space simultaneously (Figure 9, right panel).

The isochrone fitting of *Yasone-3* points to an old (12_{-2}^{+1} Gyr), metal-poor ($[\text{Fe}/\text{H}] = -2.0 \pm 0.25$) stellar population at an approximate heliocentric distance of 15_{-5}^{+3} kpc. With this tentative heliocentric distance we can estimate $M_g = 2.30_{-0.62}^{+0.48}$, $M_V = +2.52_{-0.62}^{+0.48}$, a total stellar mass of $14.4_{-5.2}^{+11.2} M_\odot$ (assuming a mass-to-light ratio in the *g*-band of 1.03) and $r_h = 2.09_{-0.42}^{+0.70} \text{ pc}$ (see Figure 4, bottom). The lowest mass star observed at the heliocentric distance of 15 kpc is $\sim 0.29 M_\odot$, implying we have observed roughly 61% of the total stellar mass in *Yasone-3* (under the assumption of a Kroupa IMF).

We also identify two *Gaia* sources within $40''$ of the candidate’s centroid (Figure 8, left panels) that align with the post main sequence turn-off part of the isochrone (Figure 8, centre panels) and are very close to each other in proper motion space (Figure 9, right panel). Due to the presence of only two *Gaia* sources —both exhibiting nearly identical proper motions—, the inferred proper motion dispersion (both in angular and physical units) is effectively zero (see Figure 9, right panel). For this reason, the corresponding entry is left blank in Table 2. However, we can still study the mean proper motion value of the two *Gaia* stars, which yield: $\mu_\alpha \cos \delta = -1.05 \text{ mas yr}^{-1}$, $\mu_\delta = -3.29 \text{ mas yr}^{-1}$, and total proper motion $\mu = -3.30 \text{ mas yr}^{-1}$. Applying our distance estimation, we obtain kinematic values: $v_\alpha \cos \delta = -7.49_{-1.50}^{+2.50} \text{ km s}^{-1}$, $v_\delta = -234_{-78}^{+47} \text{ km s}^{-1}$, and a total heliocentric tangential velocity $v_{\text{tan}} = 234_{-47}^{+78} \text{ km s}^{-1}$.

3.2 Disc Candidates

As part of our search for stellar overdensities in the *Pan-STARRS* database, we extended the sky coverage to regions with $|b| < 20^\circ$. After cross-matching with *Gaia*, we identified sixteen additional HCC candidates distributed across a broad area of the sky, spanning Galactic latitudes from $b = -4^\circ$ to $b = 7.5^\circ$ (see Figure 3, orange stars). Given their proximity to the Galactic disc, no GTC imaging was requested, as the likelihood of these systems being young open clusters —rather than old, dynamically evolved clusters possibly associated with past accretion events— was significantly higher. On top of that, most of these systems exhibit a sufficient number of *Gaia* sources that are clustered in proper motion space and aligned along a well-defined sequence in the colour–magnitude diagram, confirming their nature as compact clusters. These populations display r_h ranging from $\sim 10''$ to $\sim 30''$, and host an average of 20–40 putative stellar members (see Table 2), making them among the most compact star clusters identified to date (Kharchenko et al. 2013; Dias et al. 2014; Sánchez et al. 2018). Isochrone fitting suggests young (0.3–3 Gyr), solar to super-solar metallicity ($[\text{Fe}/\text{H}] \sim 0\text{--}0.5$) populations at heliocentric distances ranging from 1 to 15 kpc. With this, we can derive an estimated range of r_h using physical units that roughly span from 0.25 to 1.5 pc. As per the total stellar mass, we convert the total flux from all the putative members in each candidate and obtain a range of masses that spans from a few solar masses to a bit over a hundred.

Figure 10 presents the photometric and kinematic analysis of *Yasone-5*, the brightest of our disc-associated HCC candidates and the second most distant ($13.5_{-2.0}^{+0.5}$ kpc) as inferred from isochrone fitting (see Table 2). Based on these values, we estimate a physical r_h of $1.58_{-0.23}^{+0.06} \text{ pc}$, an absolute *g*-band magnitude of $-0.75_{-0.08}^{+0.35} \text{ mag}$, an absolute *V*-band magnitude of $-0.29_{-0.08}^{+0.35} \text{ mag}$ and a total stellar mass of $125_{-35}^{+10} M_\odot$, making it the largest and most massive of the disc-associated HCCs in our catalogue. Kinematically, the candidate exhibits a heliocentric tangential velocity of $54.0_{-8.0}^{+2.0} \text{ km s}^{-1}$, and

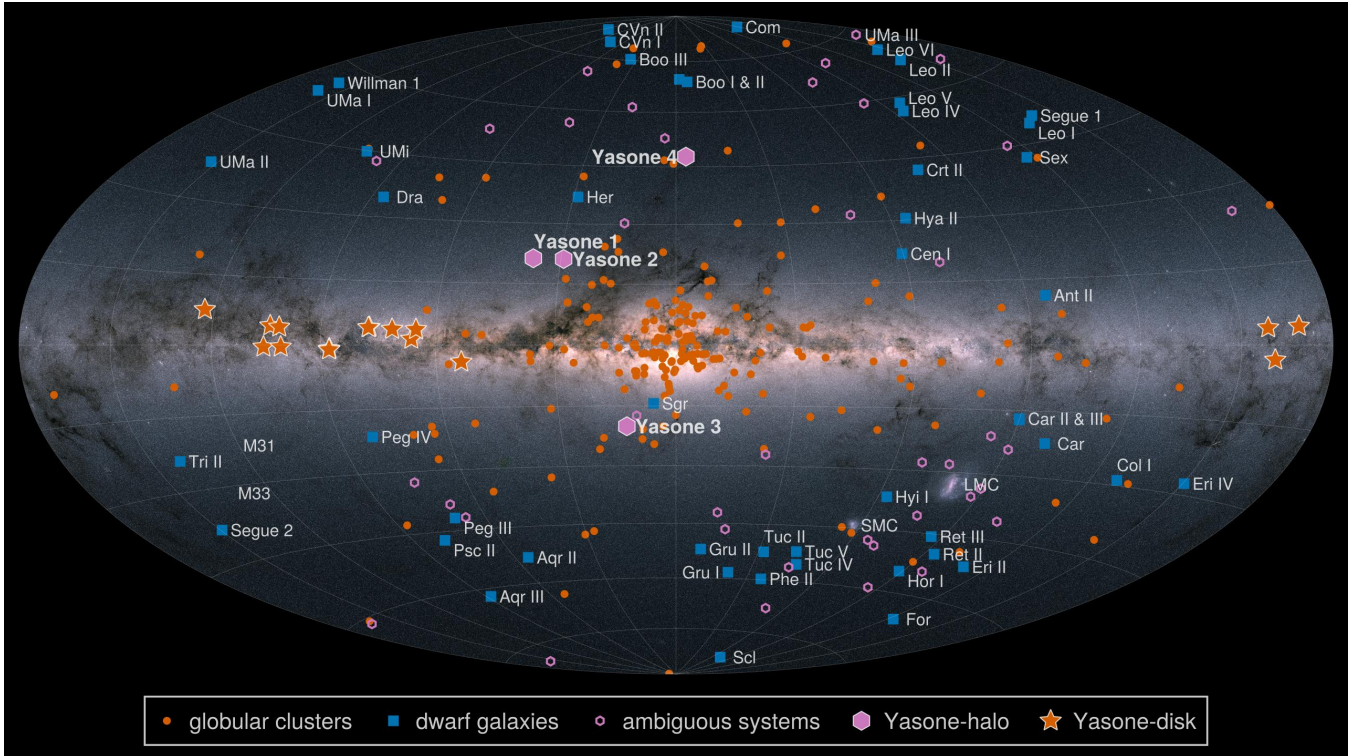


Figure 3. Sky distribution of our four halo-associated HCC candidates (*Yasone 1–4*; filled magenta hexagons) and our disc-associated candidates (*Yasone 5–20*; orange stars), overlaid on an all-sky projection of the MW in equatorial coordinates. For spatial context, we also display known GCs (orange dots), local dwarf galaxies (blue squares), and ambiguous stellar systems (open magenta hexagons) from the local volume database (Pace 2024). The background image is from ESA/Gaia/DPAC, and the locations of *Yasone 1–20* are from this work.

a proper motion dispersion that is relatively large, with a value of $\sim 20 \text{ km s}^{-1}$, though it can be reduced to $\sim 10 \text{ km s}^{-1}$ by adopting a more conservative selection criterion in proper motion space, while still retaining over 70% of the identified stellar members.

4 SUMMARY AND CONCLUSIONS

We have analyzed over 20,000 deg 2 of sky using the Pan-STARRS and HSC-SSP databases to search for compact star groupings potentially hosting IMBHs. This search has been complemented with GTC deep imaging of three candidates and astrometric data from *Gaia* Data Release 3. We identify four HCC candidates (*Yasone-1* to *Yasone-4*) in the Galactic halo; three of them (*Yasone-1* to *Yasone-3*) have been confirmed with deep photometric follow-up observations from GTC, while the fourth (*Yasone-4*) is a lower-confidence candidate identified in the HSC database. Additionally, we identify sixteen additional HCC candidates (*Yasone-5* to *Yasone-20*) close to the Galactic disc.

Yasone-1, *Yasone-2* and *Yasone-3* are identified as $>4\sigma$ stellar density outliers in the low-latitude halo $|b| \sim 20^\circ$ with main sequence structure and a kinematic overdensity in proper motion space. Isochrone fitting places them as old, low-metallicity populations at heliocentric distances in the range of 12–20 kpc and absolute magnitudes in the range $M_V = +1.8\text{--}2.5$, precluding robust classification of their nature as compact star clusters or extremely faint dwarf satellites until further spectroscopic analysis. Structurally, they are identified as associations of 40 to 50 stellar sources, most of them extremely faint ($g > 22$ mag), occupying very compact sizes with $r_h = 1.4\text{--}2.4$ pc.

Their sizes and total stellar mass lower limits of $14\text{--}28 \text{ M}_\odot$ make them very similar to the recent discovery of Ursa Major III (Smith et al. 2024), although without spectroscopic confirmation, their nature as UFDs or faint self-gravitating star clusters remains to be determined. Although *Yasone-2* displays the largest size of the three ($2.44^{+1.22}_{-1.46}$ pc), we highlight its relatively high mass ($28.0^{+35.0}_{-23.5} \text{ M}_\odot$) and tangential velocity dispersion ($59^{+30}_{-35} \text{ km s}^{-1}$) as the candidate host of a $\gtrsim 100 \text{ M}_\odot$ IMBH assuming that it has lost $\sim 80\%$ of its original mass, and that it was initially orbiting around a central BH of equal mass (see O’Leary & Loeb 2012; Rashkov & Madau 2013). Note, however, that the proper motion dispersion quoted above is strictly an upper limit, since the intrinsic proper motion errors from *Gaia* can be larger than those derived from *Gaia* proper motion uncertainties (see Vasiliev & Baumgardt 2021).

One possible IMBH indicator is the ratio between a cluster’s core radius r_c and its r_h , with values $r_c/r_h > 0.5$ suggested as indicative of IMBH-driven core inflation (Hurley 2007). Although r_c can, in principle, be derived from the surface brightness profile without spectroscopic data, in practice, the limited number of detected member stars (e.g., ~ 30) introduces significant Poisson noise, resulting in large uncertainties that hinder robust profile fitting and core radius determination.

We identify sixteen additional HCC candidates (*Yasone-5* to *Yasone-20*) scattered throughout Galactic latitudes $b = -4^\circ$ to 7.5° and heliocentric distances 1–15 kpc with typical ages 0.3–3 Gyr and solar to super-solar metallicities, making them likely open cluster candidates with similar sizes to those found in the halo. We highlight *Yasone-5* as a representative of this subsample, the brightest ($M_V = -0.29^{+0.35}_{-0.08}$ mag) and most massive ($125^{+10}_{-35} \text{ M}_\odot$) of

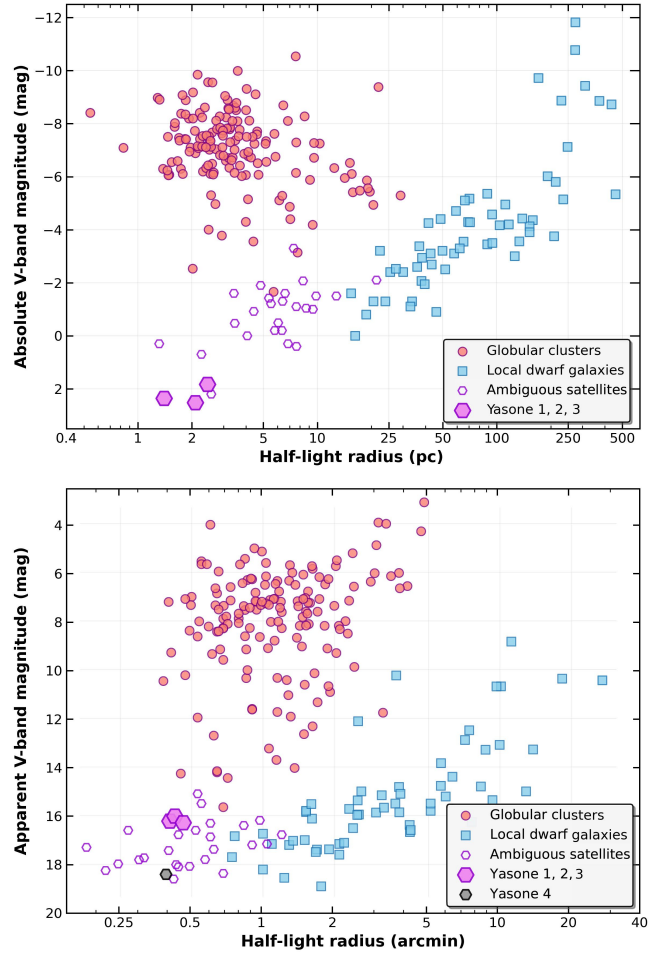


Figure 4. Top: Absolute V-band magnitude as a function of r_h in parsecs. Bottom: Apparent V-band magnitude as a function of r_h in arcminutes. In both panels, our halo-associated HCC candidates (filled magenta hexagons) are shown alongside known GCs (red circles), local dwarf galaxies (blue squares), and ambiguous stellar systems (open magenta hexagons) from the local volume database (Pace 2024).

our disc-associated HCCs, with a heliocentric tangential velocity of 54.0 ± 2.0 km s $^{-1}$.

Finally, the detection of numerous compact stellar systems in this work suggests that the search for HCCs in Galactic latitudes $|b| < 20$ using existing surveys such as Pan-STARRS and *Gaia* is far from complete. Concurrently, if a deep, wide-field survey with the imaging depth and spatial resolution of HSC Subaru were to extend its sky coverage significantly, we would expect a sharp increase in the discovery of faint, compact star clusters, similar to HSC-1, and low-luminosity MW satellites such as Boötes IV (Homma et al. 2019). This highlights the considerable discovery space that remains for low-mass and low-luminosity systems in the Local Volume. In the meantime, further efforts should focus on the low-latitude regions of the halo ($|b| \sim 20^\circ$), where the balance between sufficient stellar number density and reduced foreground contamination creates a promising window for detecting old and dynamically evolved systems that may retain imprints of MW's merging history, or even the high-redshift Universe.

ACKNOWLEDGEMENTS

M.M. acknowledges support from the Spanish Ministry of Science and Innovation through the project PID2021-124243NB-C22. This project was also partially supported by the program Unidad de Excelencia María de Maeztu CEX2020-001058-M. N.B. and S.B. acknowledge support from the Spanish Ministerio de Ciencia e Innovación through project PID2021-124243NB-C21. J.F.N. acknowledges the hospitality of the Max-Planck Institute for Astrophysics, of the Donostia International Physics Center, and of Durham University, during the completion of this research.

The Pan-STARRS1 Surveys and the PS1 public science archive have been made possible through contributions by the Institute for Astronomy, the University of Hawaii, the Pan-STARRS Project Office, the Max-Planck Society and its participating institutes, the Max Planck Institute for Astronomy, Heidelberg and the Max Planck Institute for Extraterrestrial Physics, Garching, The Johns Hopkins University, Durham University, the University of Edinburgh, the Queen's University Belfast, the Harvard-Smithsonian Center for Astrophysics, the Las Cumbres Observatory Global Telescope Network Incorporated, the National Central University of Taiwan, the Space Telescope Science Institute, the National Aeronautics and Space Administration under Grant No. NNX08AR22G issued through the Planetary Science Division of the NASA Science Mission Directorate, the National Science Foundation Grant No. AST-1238877, the University of Maryland, Eotvos Lorand University (ELTE), the Los Alamos National Laboratory, and the Gordon and Betty Moore Foundation.

This research is based [in part] on data collected at the Subaru Telescope, which is operated by the National Astronomical Observatory of Japan. We are honored and grateful for the opportunity of observing the Universe from Maunakea, which has the cultural, historical, and natural significance in Hawaii.

This work has made use of data from the European Space Agency (ESA) mission *Gaia* (<https://www.cosmos.esa.int/gaia>), processed by the *Gaia* Data Processing and Analysis Consortium (DPAC, <https://www.cosmos.esa.int/web/gaia/dpac/consortium>). Funding for the DPAC has been provided by national institutions, in particular the institutions participating in the *Gaia* Multilateral Agreement.

This work used data obtained with the OSIRIS instrument on the GTC, installed at the Spanish Observatorio del Roque de los Muchachos of the Instituto de Astrofísica de Canarias, on the island of La Palma. The GTC project is a partnership of the Instituto de Astrofísica de Canarias, the Universidad Nacional Autónoma de México, and the University of Florida in the USA. The observations were carried out under program ID GTC73-23A and reduced utilizing SAUSERO (Pérez-Toledo 2025).

DATA AVAILABILITY

This work makes use of the MESA Isochrones & Stellar Tracks software, available at <https://waps.cfa.harvard.edu/MIST/index.html> (Choi et al. 2016; Dotter 2016)

REFERENCES

Abazajian K. N., et al., 2009, The Astrophysical Journal Supplement Series, 182, 543
 Abuter R., et al., 2019, Astronomy & Astrophysics, 625, L10

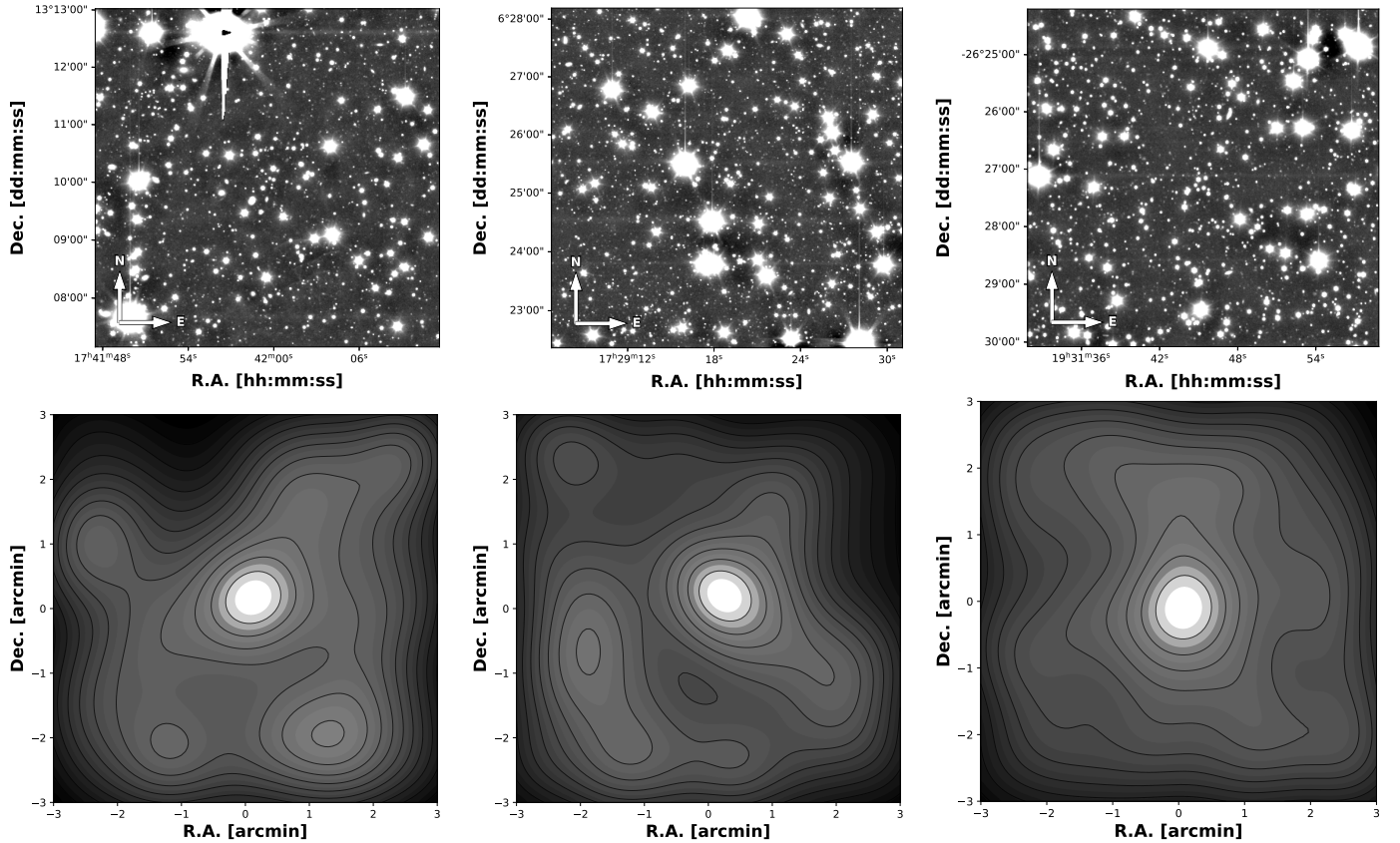


Figure 5. Top panels: $6' \times 6'$ cutouts of GTC g -band observations centered on stellar cluster candidates *Yasone-1* (left), *Yasone-2* (center), and *Yasone-3* (right). The images are displayed with logarithmic scaling to highlight stellar concentrations. **Bottom panels:** Smoothed spatial density maps within the corresponding $6' \times 6'$ fields of view. Density enhancements trace the spatial structure of the cluster candidates. All panels share the same angular scale and are oriented with north up and east to the right.

Ahvazi N., Benson A., Sales L. V., Nadler E. O., Weerasooriya S., Du X., Bovill M. S., 2024, Monthly Notices of the Royal Astronomical Society, 529, 3387

Aihara H., et al., 2022, Publications of the Astronomical Society of Japan, 74, 247

Barrows R. S., Mezcua M., Comerford J. M., 2019, The Astrophysical Journal, 882, 181

Belokurov V., et al., 2007, The Astrophysical Journal, 654, 897

Brown A. G., et al., 2018, Astronomy & astrophysics, 616, A1

Brown A. G., et al., 2021, Astronomy & Astrophysics, 649, A1

Bullock J. S., Boylan-Kolchin M., 2017, Annual Review of Astronomy and Astrophysics, 55, 343

Cepa J., 1998, Astrophysics and space science, 263, 369

Cepa J., et al., 2000, in Optical and IR Telescope Instrumentation and Detectors. pp 623–631

Cepa J., et al., 2003, in Instrument Design and Performance for Optical/Infrared Ground-based Telescopes. pp 1739–1749

Chambers K. C., et al., 2016, arXiv preprint arXiv:1612.05560

Chambers K., et al., 2018, in American Astronomical Society Meeting Abstracts# 231. pp 102–01

Chevance M., et al., 2020, Monthly Notices of the Royal Astronomical Society, 493, 2872

Choi J., Dotter A., Conroy C., Cantiello M., Paxton B., Johnson B. D., 2016, The Astrophysical Journal, 823, 102

Cole S., Lacey C. G., Baugh C. M., Frenk C. S., 2000, Monthly Notices of the Royal Astronomical Society, 319, 168

Collaboration L., 2020, The Data Release Seven of LAMOST Low-Resolution Spectroscopic Survey (LRS), <http://dr7.lamost.org>

Dale J. E., 2015, New Astronomy Reviews, 68, 1

Di Matteo T., Ni Y., Chen N., Croft R., Bird S., Pacucci F., Ricarte A., Tremmel M., 2023, Monthly Notices of the Royal Astronomical Society, 525, 1479

Dias W., Monteiro H., Caetano T., Lépine J. R. D., Assafin M., Oliveira A., 2014, Astronomy & Astrophysics, 564, A79

Dotter A., 2016, The Astrophysical Journal Supplement Series, 222, 8

Edge A., Sutherland W., Kuijken K., Driver S., McMahon R., Eales S., Emericson J. P., 2013, The Messenger, 154, 32

Errani R., Navarro J. F., Smith S. E., McConnachie A. W., 2024, The Astrophysical Journal, 965, 20

Errani R., Walker M. G., Rozier S., Peñarrubia J., Navarro J. F., 2025, arXiv e-prints, pp arXiv–2502

Evans N. J., et al., 2009, The Astrophysical Journal Supplement Series, 181, 321

Ferrarese L., et al., 2012, The Astrophysical Journal Supplement Series, 200, 4

Flewelling H. e., et al., 2020, The Astrophysical Journal Supplement Series, 251, 7

Fragione G., 2022, in 44th COSPAR Scientific Assembly. Held 16–24 July. p. 1948

Fujii M. S., Wang L., Tanikawa A., Hirai Y., Saitoh T. R., 2024, Science, 384, 1488

Furusawa H., et al., 2018, Publications of the Astronomical Society of Japan, 70, S3

Gaburov E., Gualandris A., Portegies Zwart S., 2008, Monthly Notices of the Royal Astronomical Society, 384, 376

Giersz M., Leigh N., Hypki A., Lützgendorf N., Askar A., 2015, Monthly Notices of the Royal Astronomical Society, 454, 3150

Greene J. E., Strader J., Ho L. C., 2020, Annual Review of Astronomy and

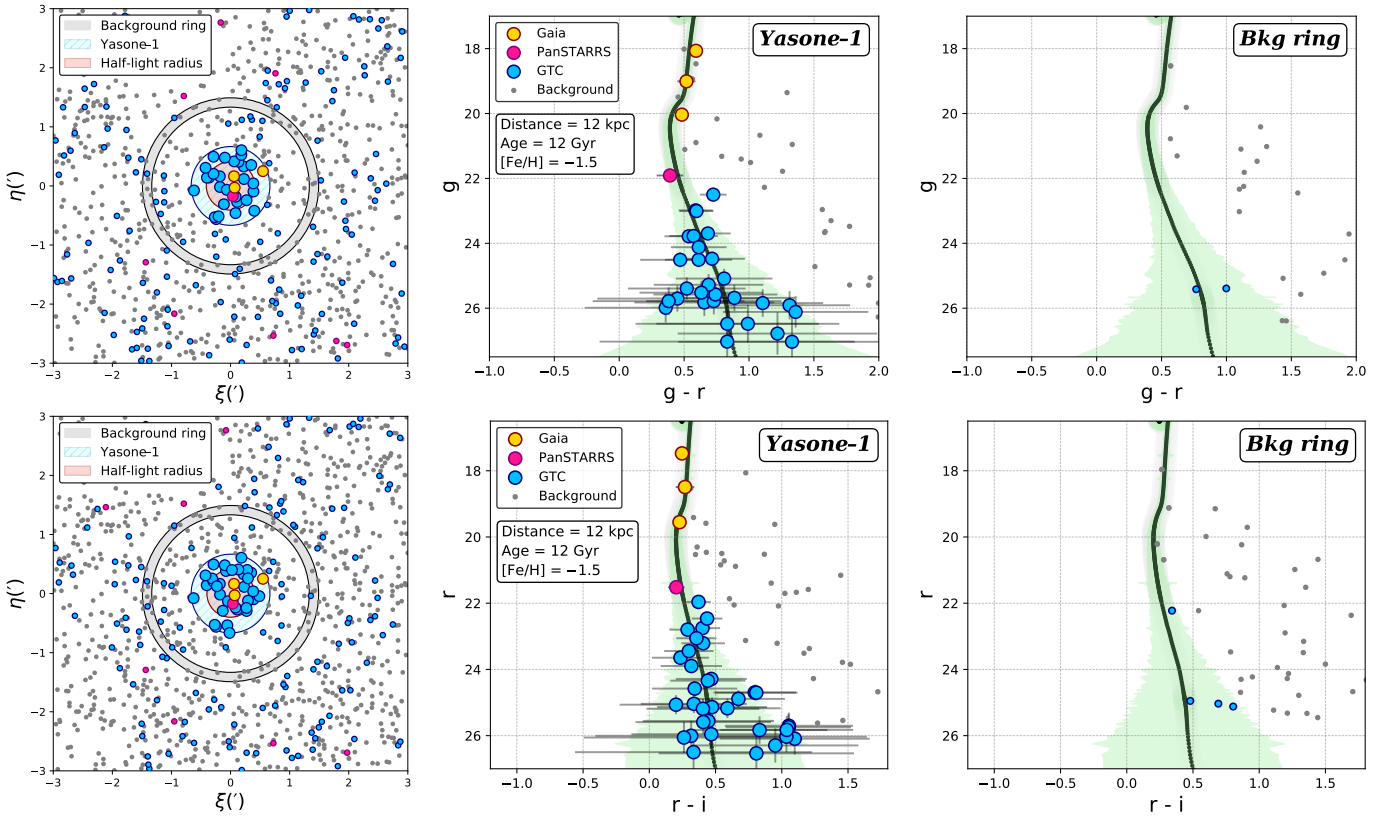


Figure 6. Photometric analysis of *Yasone-1* in the g , r bands (top row) and r , i bands (bottom row). **Left panels:** Spatial distribution of stellar sources within a $6' \times 6'$ region centered on the candidate. Enlarged dots represent stars within the candidate's $40''$ radius; smaller dots are sources beyond this radius. Colours indicate detection sources: blue (GTC only), red (GTC and Pan-STARRS), and yellow (GTC, Pan-STARRS, and *Gaia* kinematic overdensity members). Grey dots fall outside the isochrone fit. The inner circle marks the r_h ($\sim 25''$), containing half the candidate's putative members. The annulus with an inner radius of $80''$ (twice the candidate's) represents a background field region of equal area to the candidate. **Center panels:** Colour-magnitude diagrams of all stars within $40''$ radius. An old (12 Gyr), low-metallicity $[\text{Fe}/\text{H}] = -1.5$ isochrone shifted to a distance of 12 kpc is overlaid (black line) along with the sources. **Right panels:** CMDs for stars in the background annulus. All panels maintain consistent colour coding for the stellar sources.

Astrophysics, 58, 257
 Greene J. E., et al., 2021, The Astrophysical Journal, 917, 17
 Gwyn S. D., 2012, The Astronomical Journal, 143, 38
 Hodgkin S., et al., 2021, Astronomy & Astrophysics, 652, A76
 Homma D., et al., 2019, Publications of the Astronomical Society of Japan, 71, 94
 Hurley J. R., 2007, Monthly Notices of the Royal Astronomical Society, 379, 93
 Into T., Portinari L., 2013, Monthly Notices of the Royal Astronomical Society, 430, 2715
 Izquierdo-Villalba D., Colpi M., Volonteri M., Spinoso D., Bonoli S., Sesana A., 2023, Astronomy & Astrophysics, 677, A123
 Izquierdo-Villalba D., Lupi A., Regan J., Bonetti M., Franchini A., 2024, in , Black Holes in the Era of Gravitational-Wave Astronomy. Elsevier, pp 205–259
 Karim M. T., Mamajek E. E., 2016, Monthly Notices of the Royal Astronomical Society, p. stw2772
 Kawanomoto S., et al., 2018, [Publications of the Astronomical Society of Japan](#), 70
 Kharchenko N., Piskunov A., Schilbach E., Röser S., Scholz R.-D., 2013, Astronomy & Astrophysics, 558, A53
 Komiya Y., et al., 2018, Publications of the Astronomical Society of Japan, 70, S2
 Kroupa P., 2001, Monthly Notices of the Royal Astronomical Society, 322, 231
 Krumholz M. R., 2014, Physics Reports, 539, 49
 Lada C. J., Lada E. A., 2003, Annual Review of Astronomy and Astrophysics, 41, 57
 Laevens B. P., et al., 2015, The Astrophysical Journal, 813, 44
 Lee M. G., 1997, [AJ](#), 113, 729
 Lena D., Jonker P. G., Rauer J. P., Hernandez S., Kostrzewska-Rutkowska Z., 2020, Monthly Notices of the Royal Astronomical Society, 495, 1771
 Magnier E. A., et al., 2020a, The Astrophysical Journal Supplement Series, 251, 3
 Magnier E. A., et al., 2020b, The Astrophysical Journal Supplement Series, 251, 5
 Magnier E. A., et al., 2020c, The Astrophysical Journal Supplement Series, 251, 6
 Mapelli M., 2016, Monthly Notices of The Royal Astronomical Society, 459, 3432
 Marleau F. R., et al., 2024, Astronomy & Astrophysics, 690, A339
 Martin N. F., de Jong J. T., Rix H.-W., 2008, The Astrophysical Journal, 684, 1075
 Merritt D., Schnittman J. D., Komossa S., 2009, The Astrophysical Journal, 699, 1690
 Mezcua M., 2017, International Journal of Modern Physics D, 26, 11
 Mezcua M., 2019, Nature Astronomy, 3, 6
 Mezcua M., Domínguez Sánchez H., 2024, Monthly Notices of the Royal Astronomical Society, 528, 5252
 Mezcua M., Domínguez Sánchez H., 2025, Monthly Notices of the Royal Astronomical Society, 536, 295
 Miyazaki S., et al., 2018, Publications of the Astronomical Society of Japan, 70, S1
 O'Leary R. M., Loeb A., 2009, Monthly Notices of the Royal Astronomical Society, 395, 781
 Offner S. S., Clark P. C., Hennebelle P., Bastian N., Bate M. R., Hopkins P. F.,

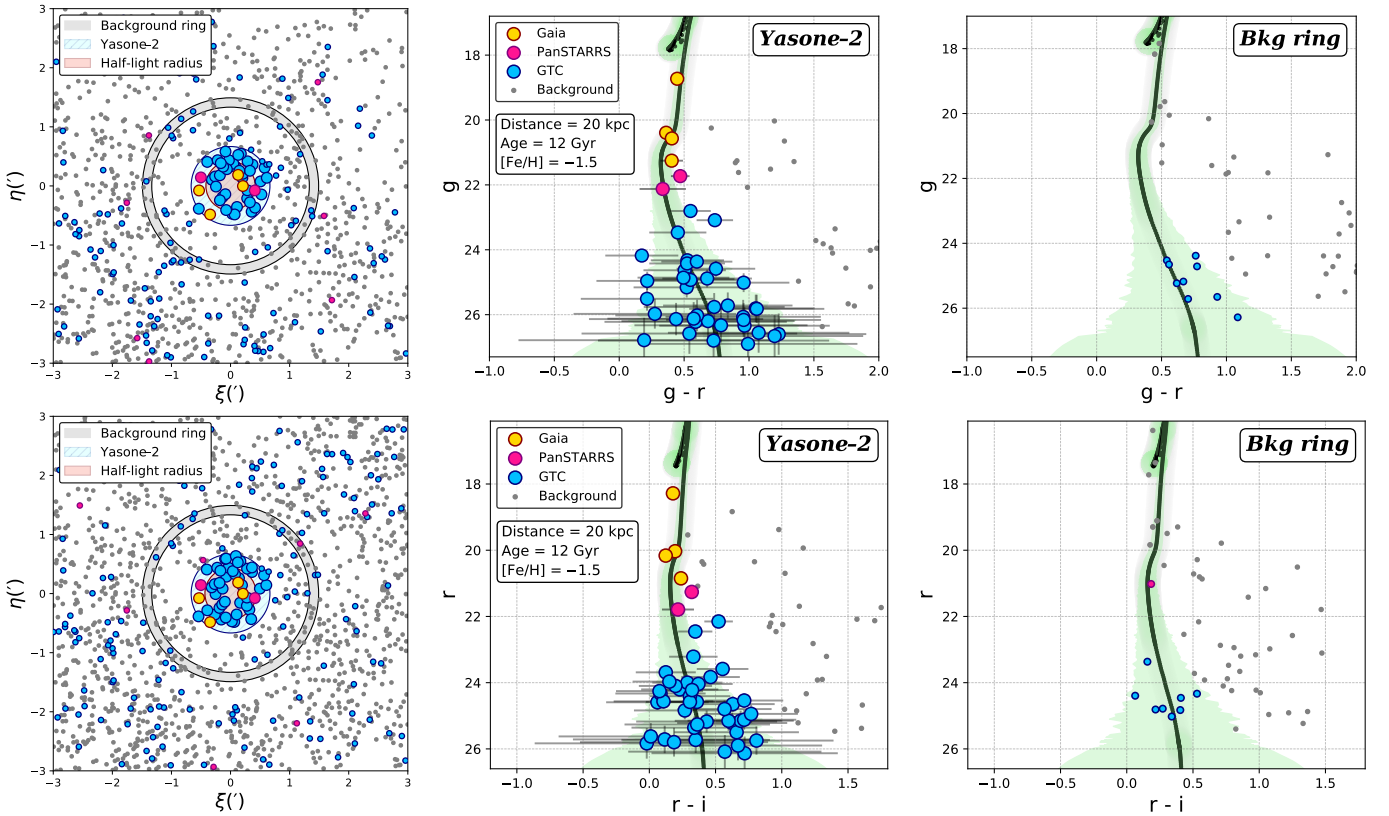


Figure 7. Photometric analysis of *Yasone-2* using the $g-r$ colour (top row) and the $r-i$ colour (bottom row). Panel layout, colour coding, and symbol definitions follow those in Fig. 6. The overlaid isochrone corresponds to an old (12 Gyr), low-metallicity ($[Fe/H] = -1.5$) stellar population at a distance of 20 kpc.

Moraux E., Whitworth A. P., 2014, *Protostars and Planets VI*, 53

O’Leary R. M., Loeb A., 2012, *Monthly Notices of the Royal Astronomical Society*, 421, 2737

Pace A. B., 2024, arXiv e-prints, pp arXiv–2411

Paxton B., Bildsten L., Dotter A., Herwig F., Lesaffre P., Timmes F., 2010, *The Astrophysical Journal Supplement Series*, 192, 3

Paxton B., et al., 2013, *The Astrophysical Journal Supplement Series*, 208, 4

Paxton B., et al., 2015, *The Astrophysical Journal Supplement Series*, 220, 15

Prieto E. G., Kremer K., Fragione G., Martinez M. A., Weatherford N. C., Zevin M., Rasio F. A., 2022, *The Astrophysical Journal*, 940, 131

Prusti T., et al., 2016, *Astronomy & astrophysics*, 595, A1

Pérez-Toledo F. M., 2025, *Kennicutt/SAUSERO: SAUSERO v1.0.0*, doi:10.5281/zenodo.15855515, <https://doi.org/10.5281/zenodo.15855515>

Rashkov V., Madau P., 2013, *The Astrophysical Journal*, 780, 187

Reinoso B., Latif M., Schleicher D., 2025, arXiv preprint arXiv:2503.20415

Rizzuto F. P., et al., 2021, *Monthly Notices of the Royal Astronomical Society*, 501, 5257

Sánchez N., Alfaro E. J., Lopez-Martinez F., 2018, *Monthly Notices of the Royal Astronomical Society*, 475, 4122

Schlegel D., et al., 2021, in *American Astronomical Society Meeting Abstracts*, pp 235–03

Simon J. D., 2019, *Annual Review of Astronomy and Astrophysics*, 57, 375

Skrutskie M. F., et al., 2006, *The Astronomical Journal*, 131, 1163

Smith S. E., et al., 2024, *The Astrophysical Journal*, 961, 92

Spinoso D., Bonoli S., Valiante R., Schneider R., Izquierdo-Villalba D., 2023, *Monthly Notices of the Royal Astronomical Society*, 518, 4672

Tachibana Y., Miller A. A., 2018, *Publications of the Astronomical Society of the Pacific*, 130, 128001

Ter-Kazarian G., 2022, *Communications of the Byurakan Astrophysical Observatory*, 69, 47

Tonry J., et al., 2012, *The Astrophysical Journal*, 750, 99

Torrealba G., et al., 2018, *Monthly Notices of the Royal Astronomical Society*, 475, 5085

Urtzaga J., Bonoli S., Izquierdo-Villalba D., Mezcua M., Spinoso D., 2024, *Monthly Notices of the Royal Astronomical Society*, 535, 3293

Vallenari A., Brown A., Prusti T., 2022, *Astronomy & Astrophysics*

Vansevičius V., Kodaira K., Narbutis D., Stonkutė R., Bridžius A., Deveikis V., Semionov D., 2009, *The Astrophysical Journal*, 703, 1872

Vasiliev E., Baumgardt H., 2021, *Monthly Notices of the Royal Astronomical Society*, 505, 5978

Waters C., et al., 2020, *The Astrophysical Journal Supplement Series*, 251, 4

Weller E. J., Pacucci F., Hernquist L., Bose S., 2022, *Monthly Notices of the Royal Astronomical Society*, 511, 2229

Willman B., Strader J., 2012, *The Astronomical Journal*, 144, 76

Willman B., et al., 2005, *The Astronomical Journal*, 129, 2692

Willmer C. N., 2018, *The Astrophysical Journal Supplement Series*, 236, 47

Wu H., Yuan H., Wang Y., Niu Z., Zhang H., 2024, *The Astronomical Journal*, 167, 277

Zwart S. F. P., McMillan S. L., 1999, *The Astrophysical Journal*, 528, L17

de Jong J. T., et al., 2015, *Astronomy & Astrophysics*, 582, A62

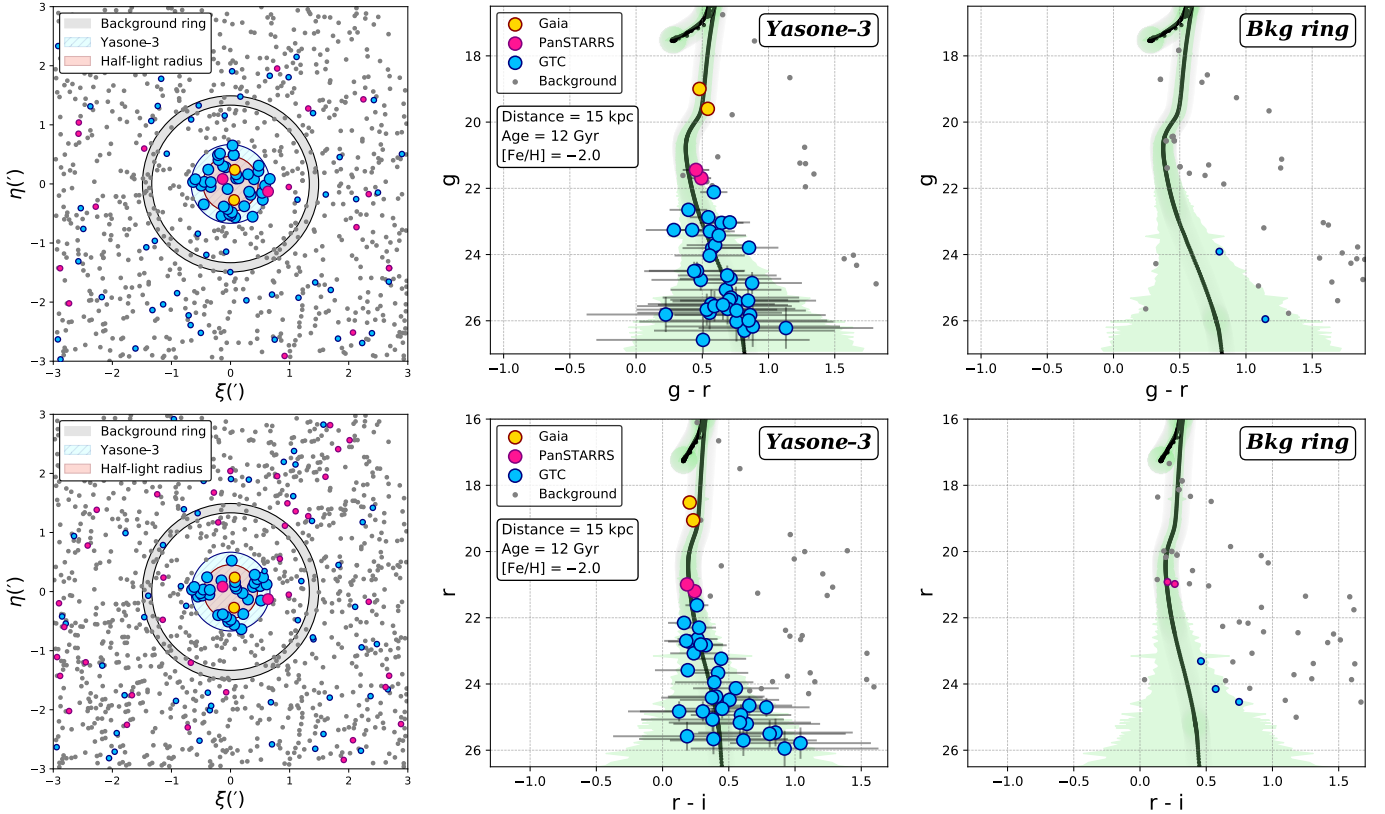


Figure 8. Photometric analysis of *Yasone-3* using the $g-r$ colour (top row) and the $r-i$ colour (bottom row). Panel layout, colour coding, and symbol definitions are as in Fig. 6. The overlaid isochrone represents an old (12 Gyr), very low-metallicity ($[Fe/H] = -2.0$) stellar population at a distance of 15 kpc.

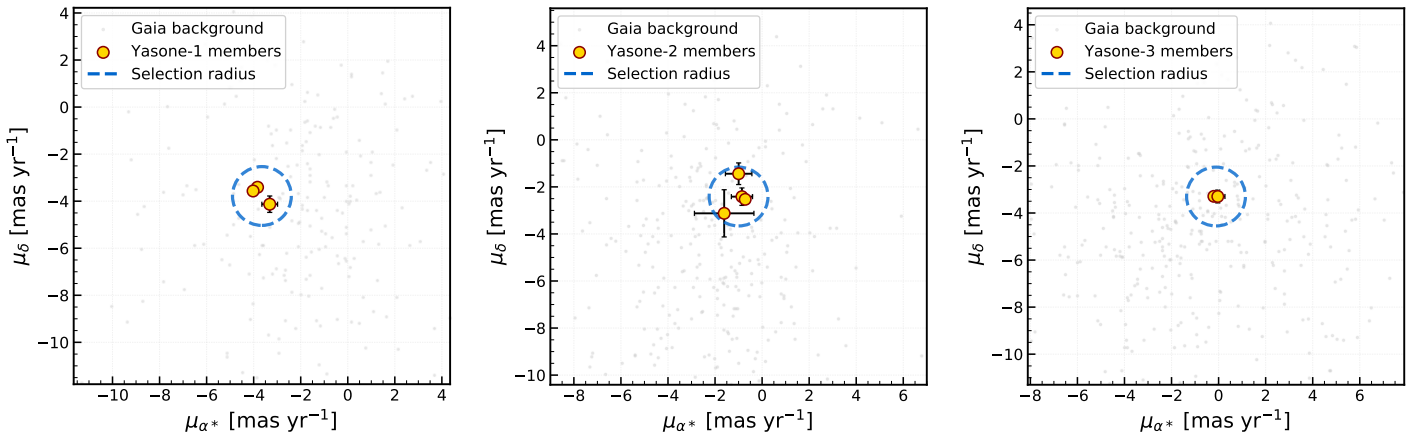


Figure 9. Proper motion distribution of stellar members associated with *Yasone-1* (left), *Yasone-2* (center), and *Yasone-3* (right), as identified from *Gaia* data. Yellow points represent stellar members identified as part of kinematic overdensities in each cluster candidate. Gray dots show all *Gaia* sources within a $6' \times 6'$ field centered on the respective candidate. The blue dashed circle indicates a 1.25 mas yr^{-1} selection radius.

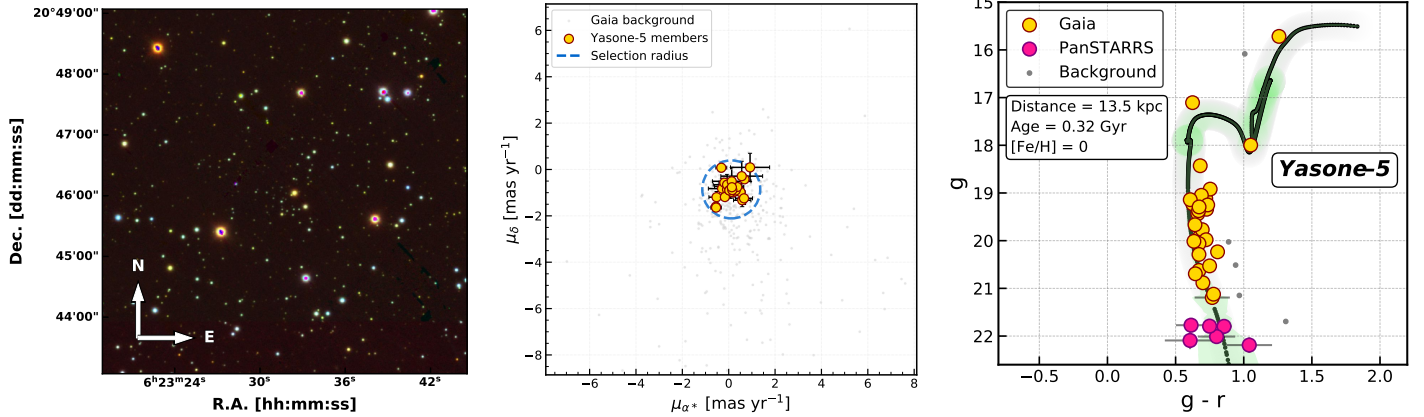


Figure 10. Photometric and kinematic analysis of *Yasone-5*. **Left:** $6' \times 6'$ cutout of a Pan-STARRS image created by stacking the y , i , and g bands, oriented with north up and east to the right. **Center:** Proper motion distribution of stellar members associated with *Yasone-5* within a $6' \times 6'$ region centered on the candidate. The colours, symbols and measures used are the same as in Fig. 9. **Right:** CMD using the g , r bands of all stars within a $45''$ radius centered on the candidate cluster. A young ($10^{8.5}$ years), solar metallicity $[\text{Fe}/\text{H}] = 0$) isochrone shifted to a distance of 13.5 kpc is overlaid (black line) along with the stellar sources. The colours, symbols and measures used are the same as in Fig. 6, but with an absence of GTC data.